Chemical Physics Impact 8 (2024) 100542

Contents lists available at ScienceDirect

Chemical Physics Impact

journal homepage: www.sciencedirect.com/journal/chemical-physics-impact

Full Length Article

Green synthesis and characterizations of magnetic iron oxide nanoparticles using *Moringa oleifera* extract for improved performance in dye-sensitized solar cell

Gabriel Ayinde Alamu [a], Paul Sola Ayanlola [a], Khadijat Kuburat Babalola [b], Oluwaseun Adedokun [a,c,*], Yekinni Kolawole Sanusi [a,c], Gabriel Ray Fajinmi [a]

[a] *Department of Pure and Applied Physics, Ladoke Akintola University of Technology, P.M.B. 4000, Ogbomoso, Nigeria*
[b] *Department of Physical and Chemical Sciences, Federal University of Health Sciences, Ila-Orangun, Nigeria*
[c] *Nanotechnology Research Group, Ladoke Akintola University of Technology, P.M.B. 4000 Ogbomoso, Nigeria*

ARTICLE INFO

Keywords:
Green synthesis
Fe_3O_4 nanoparticle
Titanium (IV) oxide (TiO_2)
Photoanode, Natural dye
Dye-sensitized solar cell

ABSTRACT

In this study, *Moringa oleifera* extract was used for the green synthesis of magnetic Iron Oxide (Fe_3O_4) nanoparticle. Natural dye from air-dried *Carica papaya* leaves was used as sensitizer along with commercially obtainable N719 Ruthenium dye. The optical absorptions between 350 and 650 nm confirmed the formation of the nanoparticle. After adding the nanoparticle to the TiO_2 and loading it with dye, the absorbance in the visible range dramatically increased. The formation and stabilization of the nanoparticle may have been aided by the functional groups, according to the FTIR results. With an average crystallite size of 35.13 nm, the XRD patterns demonstrated the nanoparticle's crystalline nature. The morphologies of the nanoparticle demonstrated that it was well-formed and homogeneously dispersed. The presence of iron and other component elements was confirmed by the EDX spectra. The production of 40.83 nm-sized nanoparticles on average was further verified by the TEM micrograph, and the samples' crystallographic planes were identified by the SAED patterns. The photo-electrochemical performance of the DSSCs showed that the efficiencies increased significantly with percentage increase of 90.1% and 89.3% for *Carica papaya* and Ruthenium dyes, respectively. The green-synthesized Fe_3O_4 nanoparticle exhibited good properties for application in DSSC.

1. Introduction

Nanoparticles are particles based on structures with characteristic features on the nanometer scale. They usually have some resemblance to their bulk counterpart based on the same atoms, but they are modified to such an extent that they have acquired superior mechanical, thermal, electrical, magnetic and optical properties. Particle size, size distribution, and morphology are examples of distinct uniqueness that give nanoparticles their novel or improved properties. Recent years have seen amazing advancements in the field of nanotechnology, with a variety of techniques being developed for the synthesis of nanoparticles with specific sizes and shapes based on needs and requirements [1]. For instance, Shanbhag et al., (2021) used SiO_2 coated Calcium titanates ($CaTiO_3$) to synthesize nanoparticles which led to controlled particles size resulting in the enhancement of their photocatalytic and electrochemical properties [2–4]. Also, Yogananda *et al.*, (2018) reported the synthesis of Sm^{3+} doped MoO_3 nanostructures (NSs) effectively by hydrothermal route using lysine as surfactant. The average quantum efficiency and color purity values of the prepared samples were found to be ~79.61% and 97% respectively. The CIE color coordinates confirmed that the phosphor emits orange-red light, which were quite useful for the fabrication of white light emitting diodes [5]. In another work, Naik et al., (2019) reported Nd^{3+} (1–9 mol%) doped Mg_2SiO_4 nanophosphors by solution combustion method and the fingerprint detection and TL properties of the nanophosphors were studied in detail to understand the suitability of the prepared phosphors for solid state display devices, forensic and dosimetry applications. The optimized product was utilized for the visualization of Latent Finger print (LFP) on versatile surfaces [6]. In related research carried out by Shanbhag et al. (2019), Li^+ (0.25–1.0 mol%) co-doped $CaTiO_3$:Sm^{3+} (3 mol%) nanoparticles (NPs) and SiO_2@$CaTiO_3$:Sm^{3+} (3 mol%), Li^+(0.25–1.0 mol%) core–shell NPs were synthesized via facile combustion technique using Oxalyl

---

* Corresponding author at: Department of Pure and Applied Physics Ladoke Akintola University of Technology, P.M.B 4000 Ogbomoso, Nigeria.
E-mail addresses: oadedokun@lautech.edu.ng, adedokunoluwaseun2@gmail.com (O. Adedokun).

https://doi.org/10.1016/j.chphi.2024.100542
Received 12 December 2023; Received in revised form 19 January 2024; Accepted 16 February 2024

Dihydrazide (ODH) as a fuel. All the obtained results suggested that the mentioned nanophosphors provided a platform for fabricating other new functional materials which can be applied in the field of W-LEDs, biological imaging and solid state display applications [7].

Recently, research groups in many areas of endeavor have been zealously concerned with magnetic Iron Oxide (Fe_3O_4) nanoparticles due to the fact that they have unique properties and extensive applications [8]. The magnetic Fe_3O_4 nanoparticle is most commonly explored due to its well-crystalline nature, excellent thermodynamic stability, and, outstandingly, its superparamagnetic behavior [9]. When Fe_3O_4 magnetic nanoparticles' particle size drastically decreases at room temperature, they exhibit superparamagnetic behavior, which is similar to that of a magnetic dipole with a permanent magnetic moment that is easily affected by an external magnetic field. Both its enormous magnetic susceptibility and smaller size make Fe_3O_4 nanoparticle a potential candidate for being integrated in photovoltaic devices [10].

But, synthesized Fe_3O_4 nanoparticles through physical and chemical routes tend to be extremely reactive and create aggregates that ultimately cause reactivity to disappear [11]. Also, the synthesized Fe_3O_4 nanoparticles using traditional techniques are not applicable in areas where nonpolar organic solvents are utilized since their exposure to air will make them lose their magnetism and dispersibility [12]. Researchers now pay a lot of attention to green nanotechnology in order to reduce or get rid of harmful materials and revitalize the surroundings. Eco-friendly, harmless, and non-toxic ingredients are usually used when it comes to green nanoparticle synthesis [13] and the improvement of dependable, non-toxic, and environmentally friendly routes for the synthesis of magnetic Fe_3O_4 nanoparticles is crucial to expanding their range of uses [11]. It has been proposed that environmentally friendly alternatives to chemical and physical methods for the synthesis of nanoparticles include the use of microorganisms, enzymes, fungi, and plants or plant extracts [14]. Aside from energy efficiency, other factors to take into account when implementing a greener technique are availability, affordability, environmental friendliness, and pollution reduction [15]. When compared to nanoparticles made by physical and chemical means, biosynthesized ones frequently exhibit reduced toxicity and particle agglomeration, as well as improved stability because the bioactive components (mostly polyphenols) of those biological materials exhibit stabilizing and capping effects, particularly plants [16]. At times, it is highly beneficial to prepare nanoparticles using plants or plant parts as a way of the elimination of the complex labor required to maintain microbial cultures [14].

Currently, improvements are being made to the biosynthesis of magnetic Fe_3O_4 nanoparticles by plants, and their production from inactivated plant tissue, plant extracts, exudates, and other parts of living plants is being investigated. Plants are explored for biosynthesis because they are reported to contain reducing agents that may play significant roles in the biosynthesis of Fe_3O_4 nanoparticles [14]. Medicinal plants can easily be combined with magnetic Fe_3O_4-based nanoparticles for many uses because they provide good formulations that yield to multiple biological signaling processes [17]. One of the numerous plants with a green synthesis inspiration is *Moringa oleifera*, whose high concentration of bioactive and antioxidant substances have long been utilized to treat bacterial and viral infections, cancer, and inflammation. It is a fantastic synthesis instrument for the necessary nanoparticles because it is exceptionally rich in such polyphenols that could be used for synthesis [18].

As far as DSSC fabrication is concerned, one of the most effective photoanodes is the TiO_2-based, but, it absorbs only ultraviolet (UV) radiation, a minuscule portion of the solar spectrum. Consequently, dye molecules work as sensitizers to absorb visible light [19]. Ruthenium-based dyes as sensitizers have strong visible absorption, but their costly synthesis and undesired environmental impacts have made researchers look for natural dyes as alternatives [20]. Chlorophyll, carotene and other pigments, are unreservedly available in plant materials and fulfill the requirement as sensitizers [20]. But, the performance of natural dyes is very low compared with the Ruthenium-based dyes, which necessitates the use of nanoparticles [21]. Manikandan et al. (2015) used a one-pot low-temperature approach to create nanostructured α-Fe_2O_3-based DSSC with two morphologies: nanorods and nanoparticles. The ferromagnetic property of the as-prepared α-Fe_2O_3 samples was revealed by the magnetic measurement. Under 1000 W/m^2 of light radiation, the DSSC produced with the optimized α-Fe_2O_3 nanorods array achieved a power conversion efficiency of 0.43%, which was superior to that obtained from α-Fe_2O_3 nanoparticles (0.29%) [22]. The photovoltaic characteristics of DSSC based on Fe_3O_4–TiO_2 photoelectrode were studied by Chou et al. (2016). The Fe_3O_4–TiO_2 photoelectrode was created using the spin coating technique. The effects of adding Fe_3O_4 to the TiO_2 photoanode of a dye-sensitized solar cell (DSSC) were examined using atomic force microscopy, X-ray diffraction, UV–visible spectroscopy, and electrochemical impedance spectroscopy. Compared to the efficiency of 2.35% of the DSSC based on TiO_2 pure photoanode, a power conversion efficiency of 3.54% was achieved. The experiment's results demonstrated that Fe_3O_4 acted as a catalyst to provide a new electron channel for DSSC, lowering the requirement for charge recombination [23]. In 2021, Kamil and colleagues synthesized α-Fe_2O_3 nanoparticles through UV-irradiation, with the intention of using them in dye-sensitized solar cells. They demonstrated α-Fe_2O_3 nanoparticles produced by photolysis with UV lamb in their work. Through the use of TEM, XRD, EDX, PL, and FE-SEM, the nanopowder was examined. It was determined that the mean particle size of the α-Fe_2O_3 NPs was 25 nm. The X-ray diffraction analysis revealed no impurity peaks. The efficiency varied from 0.810% to 2.13%, and the energy gap was determined to be 2.49 eV. It has been demonstrated that adding iron oxide nanoparticles to DSSCs improves their performance [24]. Kannan et al. (2019) concluded after their investigation that $Fe^{3+}$of Fe_3O_4 nanoparticle could enhance the absorption of light from the ultraviolet to the visible spectrum [25]. Also, Liang Wang (2014) used the composite of carbon/Fe_3O_4 (bulk) as a counter electrode to enhance DSSC efficiency [26].

Green synthesized magnetic Fe_3O_4 nanoparticle has found widespread application in the photocatalyst and biomedical domains due to its exceptional dispersion, biocompatibility, and elevated specific surface area [25]. The results of this novel work revealed that, in DSSC also, the incorporation of the green-synthesized magnetic nanoparticles, which is readily available, into the TiO_2 electrode had a significant impact in improving the photogenerated electron transfer ability of the natural dyes-based photoanode semiconducting material, and reduce charge recombination. In this study, fresh moringa leaf extract was used to synthesize the Fe_3O_4 nanoparticles and their UV–vis spectroscopy, FTIR, XRD, SEM, EDX, TEM and SAED data analyses were carried out. For the purpose of fabricating the DSSC, air-dried *Carica papaya* (Pawpaw) leaves were used to extract the natural dye and its photovoltaic capability together with that of the N719 dye were assessed.

2. Experimental techniques

2.1. Materials

We used Potassium Iodide, Iron Oxide (Fe_3O_4), and Sigma-Aldrich's titanium dioxide (P25) without additional purification. *Carica papaya* (Pawpaw) and *Moringa oleifera* (Moringa) leaves were acquired from Ladoke Akintola University of Technology, Ogbomoso's Teaching and Research Farm. The N719 dye and Indium-doped Tin Oxide (ITO) conducting substrates (50 × 50 × 1.1 mm, 10 Ω/sq) were acquired from Solaronix S.A.

2.2. Green synthesis of Fe_3O_4 nanoparticles

The leaves of *Moringa oleifera* were cleaned with distilled water, dried by air, and ground into a fine powder. After boiling the powder (20 g) in 1 litre of distilled water for 30 min at 60 °C, the extract was filtered through Whatman No. 1 filter paper. Fig. 1 illustrates the preparation and fabrication procedure. 200 ml of distilled water were combined with 4.63 grams of Fe_3O_4 to create a Fe_3O_4 solution (0.1 M). The extract (2, 4, 6, 8, and 10 ml each) was then added to 10 ml of the room temperature solution. The mixture was then stirred at 25 °C using a magnetic stirrer for about 15 min at 400 rpm [27,28]. The formation of intensely colored black solutions indicated that the iron oxide nanoparticles had been synthesized successfully [29]. The samples were changed to optimize the volume of extract required for the nanoparticle's synthesis.

2.3. Preparation of natural and ruthenium dyes

After being cleaned with distilled water, the *Carica papaya* (Pawpaw) leaves were air-dried and ground into a powder. To create a homogeneous suspension, 10 grams of powder were weighed, then put into a clean bottle with 100 millilitres of absolute ethanol and shaken at 150 revolutions per minute for ten minutes. After a full day in the dark, the solution was filtered. Additionally, 0.594 g of Ruthenium (N719) powder and 100 ml of ethanol were mixed to create an ethanol solution containing 0.5 mM of N719 dye [30].

2.4. Fabrication of DSSC

Using a glass cutter, indelible marker, and ruler, the conducting glass substrates (25 mm by 25 mm) and non-conducting glass substrates (75 mm by 10 mm) were cut. After using a detergent solution to clean them, the substrates were ultrasonically rinsed in distilled water for fifteen minutes at 30 °C. Additionally, the substrates were scrubbed for 30 min at 30 °C using isopropanol acid (IPA) in an ultrasonic bath. One gram of TiO_2 powder was weighed and then added to a sanitized beaker. To separate the aggregates into smaller pieces, 2.5 millilitres of distilled water was added. After being dissolved in 5 ml of ethanol, 0.5 g of ethyl cellulose was added to the sample. Additionally, 5 millilitres of terpeneol were added, and a magnetic stirrer was used to mix the mixture. To create a homogenous paste, 50 ml of ethanol was then added gradually while the mixture was heated to 80 °C and stirred for an hour [31]. To further optimize the concentration required for cell fabrication, the pastes (1 ml each) were blended with various volume fractions of 0.5 ml, 1.0 ml, 1.5 ml, and 2.0 ml of the optimized Fe_3O_4 nanoparticle. Initially, adhesive tape was used to cover the glass substrates on two identical edges in order to control the film areas and allow electrical contact to occur in the uncoated areas. Using the doctor-blade technique, the obtained pastes were applied to the free edges of the non-conducting glass substrates [30]. After allowing them to decompress for five minutes to lessen the irregularity on the surface, they were dried at 120 °C for fifteen minutes. Using the same process, an electrode was also created without any nanoparticles as a reference. In order to prepare pastes that were deposited on ITO plates as thin films for the fabrication of the cells, optical characterizations were performed and the optimized volume of the nanoparticle was utilized. After annealing for thirty minutes at 450 °C in a furnace, the slides were left to dry before being allowed to cool to room temperature. To avoid contamination, they were subsequently housed in petridishes with adequate covering [30]. Each of the TiO_2 coated specimens were soaked into the natural and ruthenium dyes, and they were then left for eighteen hours to become sensitized. The specimens were then taken out, given an ethanol wash, allowed to air dry, and stored in sealed petridishes. To shield the specimens from direct sunlight, aluminum foil was placed over the exterior surfaces of the dishes [30]. To prepare the electrolyte, 0.83 g of Potassium Iodide (KI) and 0.127 g of Iodine were dissolved in 20 millilitres of Acetonitrile solvent [32]. To get rid of any remaining organic contaminants, other ITO glass substrates that were utilized as the cathodes were heated to 450 °C for 15 min. The conductive sides of the glass substrates were then coated with graphite nanoparticles and stored prior to use [30]. The dye sensitized solar cells were then assembled by connecting the prepared photoanodes to the counter electrodes and putting an electrolyte injection between them [30]. The two electrodes were then held together with binder clips and stored for characterization.

2.5. Characterizations

X-ray diffraction and morphology were performed on the films using a Rigaku D/Max-llC X-ray diffractometer, Scanning Electron Microscope (SEM), FEI Singshine, Hongkong, and TEM and SAED analyses on a JEM-ARM200F-G TEM unit. NICOLET iS10 spectrometer and UV–Vis spectrometer (ASUV-6300 PC and Avalight DH 5 BAL) were used to study FTIR spectrophotometry and optical absorptions, respectively. A solar simulator (Newport model No. 96000) operating at 100 mW/cm^2 (1 sun AM1.5) and 25 °C was used to measure the *J-V* characteristics along with a source measure unit(Kethley Model 2400 Source Meter).

3. Results and discussion

3.1. Optical studies

3.1.1. Optical absorbance of the synthesized Fe_3O_4 nanoparticle

Fig. 2 displays the Fe_3O_4 nanoparticle's UV–Vis optical absorptions that were synthesized using varying amounts of moringa leaf extract as a

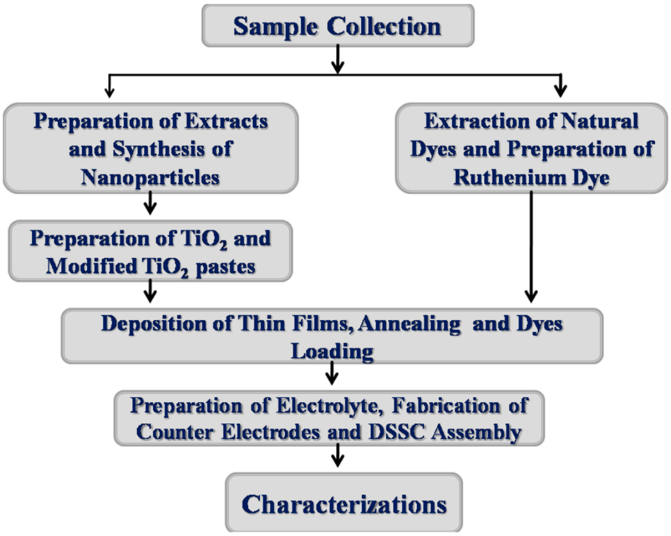

Fig. 1. Schematic figure showing the preparation and fabrication procedures.

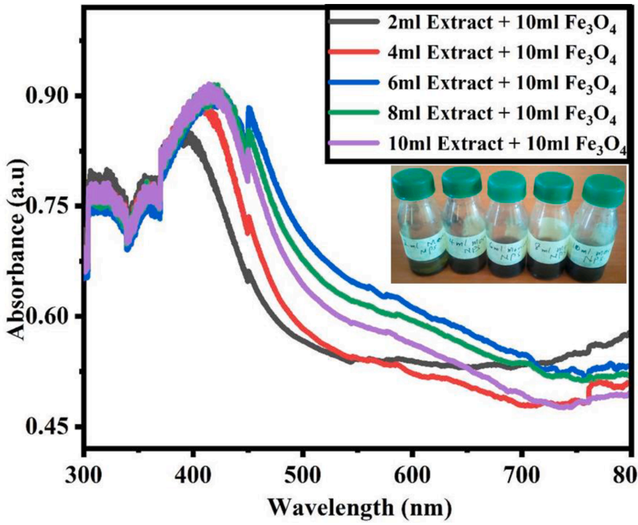

Fig. 2. Optical absorbance of the synthesized nanoparticle.

reducing agent. The nanoparticle was synthesized at different concentrations of leaves extract, ranging from 2 ml to 10 ml, at the intervals of 2 ml, using 10 ml of 0.1 M of Fe_3O_4 solution. Colour change in precursor solution confirmed the formation of the nanoparticle [29]. As the leaves extract and the Fe_3O_4 solution were mixed together, the colour changed gradually from brown to black, as shown in the inset in Fig. 2. The black colour became intense as the volume of the extract increased. The resulting intense black colored solutions confirmed the synthesis of Fe_3O_4 nanoparticle [29]. The optical absorptions observed between 350 nm and around 600 nm belong to Fe_3O_4 nanoparticle, as reported in literature [33–35]. The absorbance peaks increased gradually as the volume of the extract increased up to 6 ml. However, the absorbance peak decreased when the extract's volume was increased to 8 ml, indicating that just 6 ml of the extract were required for the nanoparticle's synthesis. As a result, the nanoparticle was successfully synthesized using 10 millilitres of 0.1 M Fe_3O_4 solution combined with 6 millilitres of the extract. In order to optimize the concentration required to be incorporated into the DSSC photoanode in order to fabricate the solar cells, the nanoparticle synthesized with 6 ml of the extract was later used for the fabrication of thin films.

3.1.2. Optical absorbance of dyes

Fig. 3(a) displays the optical absorbance spectra of the natural dye that was extracted from *Carica papaya* (Pawpaw) leaves. The goal of the absorption study was to identify the potentially useful pigments in the alcoholic extract. In the inset of Fig. 3(a), the extracted natural dye is also displayed. Fig. 3(a) illustrates the two primary strong absorption peaks of the natural dye, which are primarily concentrated at wavelengths of 411 nm and 665 nm. Additionally, two faint bands are discernible at 536 nm and 608 nm. The comparable literature data for Pheophytin 'a' is consistent with the observed strong Soret and Q bands as well as weak bands located in the spectral range between the Soret and Qy bands [20]. The soret band exhibits bathochromic shift, also known as red shift.The majority of the observed peaks match the reported band for pheophytin "a," indicating that pheophytin "a" is the most dominant pigment. Other accessory pigments of non-chlorophyll, such as caroteniods, also absorb light in addition to chlorophyll and its derivative [20]. Additionally, Fig. 3(b) displays the N719 Ruthenium dye's UV–Vis optical absorption that was prepared using ethanol as the solvent. This dye has a maximum absorption wavelength of 533 nm and an absorption band that stretches from approximately 450 nm to 600 nm. It is an impressive sensitizer for both homogeneous and heterogeneous redox reactions due to its broad range of visible light absorption and relatively long excited state [36]. It follows that photon energy in the visible portion of the electromagnetic spectrum can be absorbed by both natural and Ruthenium dyes.

3.1.3. TiO_2 film samples' optical absorbance combined with natural dye and nanoparticles

Fig. 4(a) displays the TiO_2 film samples' UV–Vis optical absorption spectrum both with and without Fe_3O_4 nanoparticles synthesized with extract from moringa leaves. To further optimize the precise volume of the nanoparticles required for the construction of the solar cells, the nanoparticles synthesized with the optimized volume (6 ml) of the extract was also varied (0.5 ml, 1.0 ml, 1.5 ml, and 2.0 ml) using the same amount of TiO_2 paste (1.0 ml). The TiO_2 paste without nanoparticles did not exhibit any absorbance in the visible region, as seen in Fig. 4(a). Because of the nanoparticle's surface plasmon resonance band, mixing it with TiO_2 paste increased its absorbance in the visible spectrum [35]. Up to 1.5 millilitres, the absorbance rose as the nanoparticle concentration rose. The absorbance peak decreased when the nanoparticle concentration was raised to 2 ml, indicating that only 1.5 ml of the optimized Fe_3O_4 nanoparticle was required for the creation of the DSSCs. Fig. 5(a) displays the TiO_2 film samples' UV–Vis optical absorption that contains Fe_3O_4 nanoparticles and natural dye. The TiO_2 paste was loaded with the dye after incorporating the nanoparticle (1.5 ml of the optimized volume). Following the loading of the natural dye, the absorbance peak of the TiO_2 paste integrated with the nanoparticle greatly expanded in the wavelength range of 380–750 nm. It turns out that following the loading of the natural dye, the nanoparticle sufficiently increased the absorption in the visible region. This demonstrates an increase in the solar cell's efficiency.

3.1.4. Optical band gaps

Curves of $(\alpha h\upsilon)^2$ versus $h\upsilon$ were plotted for the thin-film optical band gaps computations. By extrapolating the line to the base line, the energy band gaps were obtained from a straight-line plot of $(\alpha h\upsilon)^2$ versus $h\upsilon$. Fig. 4(b) displays the optical band gaps for the TiO_2 paste that was combined with the created nanoparticle. The calculated energy gap of the TiO_2 thin film alone is 3.25 eV, as can be seen in Fig. 4(b). 3.10 eV is the estimated energy gap of the TiO_2 thin film that contains 0.5 ml of the nanoparticle that was created using Moringa extract. The energy gap for the 1.0 ml TiO_2 thin film was determined to be 3.05 eV. The TiO_2 thin film incorporated with 1.5 ml of nanoparticle has an energy gap of 1.70 eV, while the TiO_2 thin film incorporated with 2.0 ml of nanoparticle has an energy gap of 2.05 eV. It was evident that as the nanoparticle concentration increased up to 1.5 ml, the band gap shrank. The band gap increased when the nanoparticle concentration was raised to 2.0 ml, indicating that 1.5 ml of the optimized volume ratio needed to be added to TiO_2 paste in order to fabricate the solar cells. Fig. 5(b) displays the TiO_2 thin-film optical band gaps when combined with the nanoparticle and loaded with natural dye. It is evident from Fig. 5(b) that the TiO_2 film alone has a computed energy gap of 3.25 eV. 2.70 eV is that of the

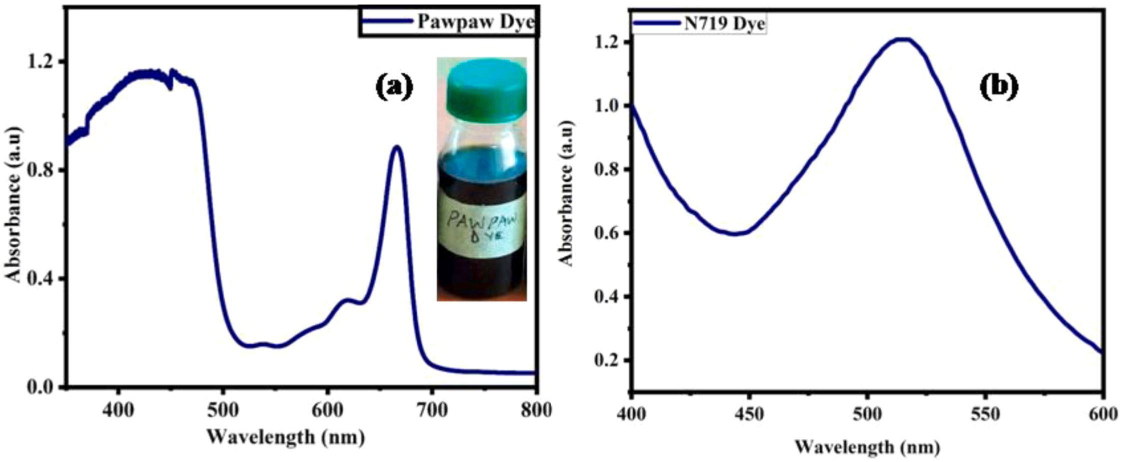

Fig. 3. Optical absorbance of the (a) natural dye(b) N719 dye.

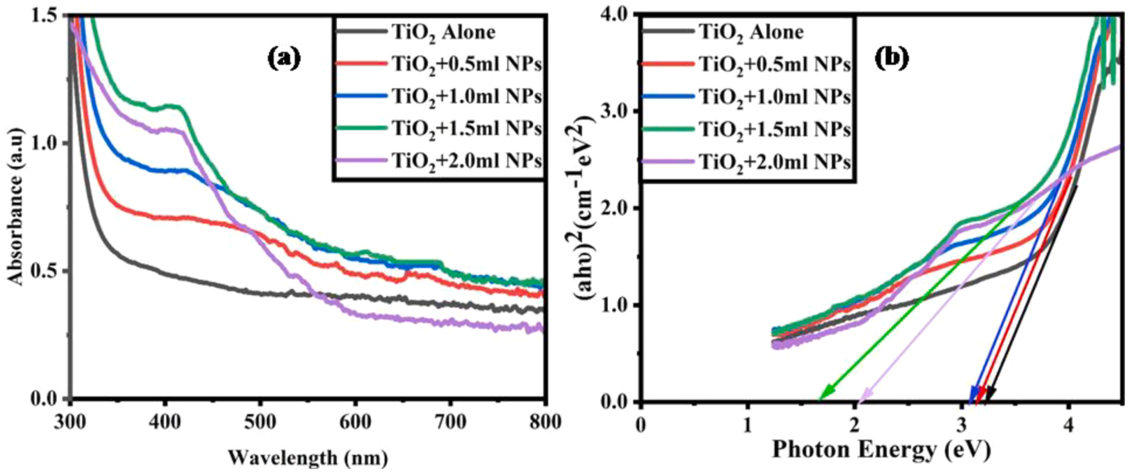

Fig. 4. (a) TiO_2 film samples' optical absorbance with the synthesized nanoparticle (b) Optical band gap of theTiO_2thin films with the synthesized nanoparticle.

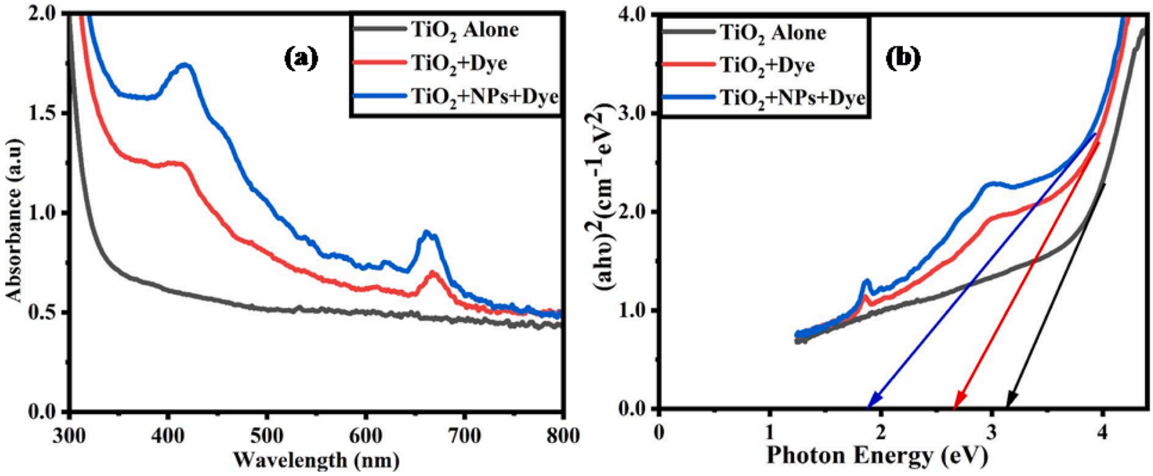

Fig. 5. (a) Optical absorbance of theTiO_2film samples with synthesized nanoparticle and natural dye (b) Optical band gap of the TiO_2 thin films with the synthesized nanoparticle and natural dye.

TiO_2 thin film that has the dye loaded in it. 1.90 eV is the energy gap of the TiO_2 thin film that has been loaded with dye and combined with the synthesized nanoparticle. The findings, which are displayed in Tables 1 and 2, suggest that as absorbance increases, the energy gap decreases. The conductivity of a material increases when the energy gap narrows because it takes less energy for electrons to reach the Fermi level of a semiconducting material [37]. Electrons in the dye molecules will be excited by the photon energy and will move from the Lowest Unoccupied Molecular Orbital (LUMO) state to the Highest Occupied Molecular Orbital (HOMO) state. The electrons will then be moved to the TiO_2 photoanode's conduction band. Therefore, for improved electron transfer to the conduction band of TiO_2 and increased fabricated DSSC efficiency, a decrease in the thin film's bandgap will be beneficial [37].

Table 1
Optical band gaps of the TiO_2 thin films with the synthesized nanoparticle.

Sample	Energy gap (eV)
TiO_2 Thin Film	3.25
TiO_2 Thin Film Incorporated with 0.5 ml Nanoparticle	3.10
TiO_2 Thin Film Incorporated with 1.0 ml Nanoparticle	3.05
TiO_2 Thin Film Incorporated with 1.5 ml Nanoparticle	1.70
TiO_2 Thin Film Incorporated with 2.0 ml Nanoparticle	2.05

Table 2
Optical band gaps of TiO_2films with the synthesized nanoparticle and natural dye.

Sample	Energy gap (eV)
TiO_2 thin film	3.25
TiO_2 thin film loaded with dye	2.70
TiO_2 thin film with the synthesized nanoparticle and loaded with dye	1.90

3.2. *FTIR spectroscopy*

3.2.1. *FTIR spectroscopy of Fe_3O_4 nanoparticle*

Fig. 6(a) displays the FTIR spectra of the extracted moringa leaves as well as the synthesized nanoparticle made from the extract. Based on Fig. 6(a), the extract's IR band at 1032 cm^{-1} is ascribed to secondary alcohols' C—OH stretching; carboxyl groups' C—C stretching vibration at 1595 cm^{-1}, protein amide I bands, and O=C=O stretching of carbon dioxide at 2360.17 cm^{-1} [38–40]. Stretching vibrations from C to H are represented by peaks at 2853.01 cm^{-1} and 2918 cm^{-1} [38]. The C=C of the naphthalene ring is responsible for the peaks at 1369 cm^{-1}, while the *N–H* group of proteins and free *O–H* stretching vibrations of alcohols are indicated by small, intense peaks at 3376 cm^{-1} and 3778.1 cm^{-1}, respectively [41,42]. As a result of metal ions interacting with Moringa

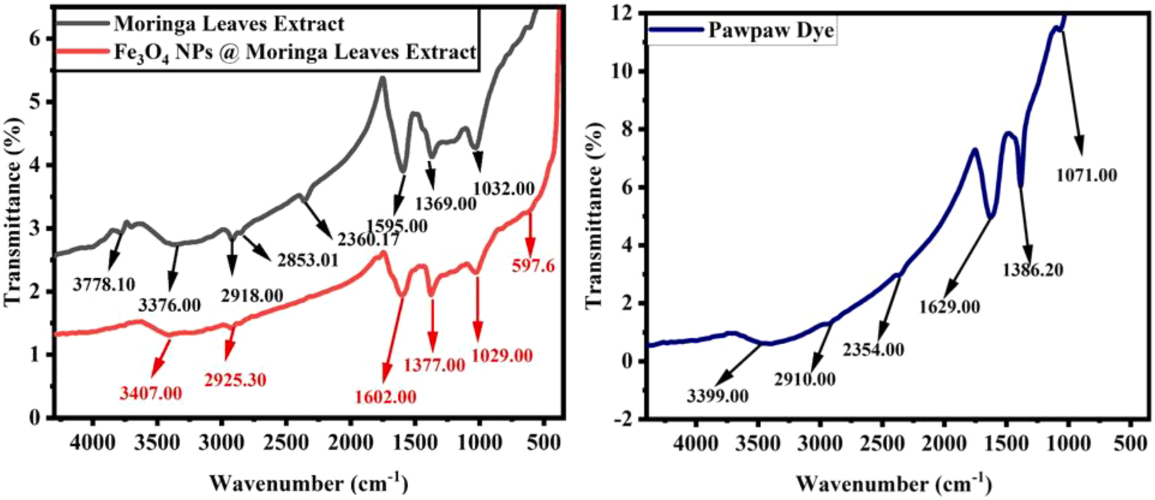

Fig. 6. FTIR spectra of the (a) moringa leaf extract and the synthesized nanoparticle (b) extracted dye.

leaves biocompounds, the Fe_3O_4 nanoparticle was reduced and stabilized, as evidenced by the IR bands seen in the synthesized nanoparticle containing extract from Moringa leaves at 3407 cm, 2925.30 cm^{-1-1}, 1602 cm^{-1}, 1377 cm^{-1}, 1029 cm^{-1}, and 597.6 cm^{-1} [43]. Furthermore, the transmittance located at 1029 cm^{-1} indicates that C–O stretching is present in the 1300 cm^{-1} and 1000 cm^{-1} region, which may be the result of ether or ester groups covalently linking with the nanoparticle [44]. The iron oxide nanoparticle's spectrum consists of the aromatic C—H stretching mode at 3407 cm^{-1}, the H—C-H bending vibration at 1377 cm^{-1}, and the C—O and C—C stretching in the 1000 cm^{-1}–1245 cm^{-1} range [45,46]. IR band shifts occur: 1032 cm^{-1} to 1029 cm^{-1}, 1369 cm^{-1} to 1377 cm^{-1}, 1595 cm^{-1} to 1602 cm^{-1}, 2918 cm^{-1} to 2925 cm^{-1}, and 3376 cm^{-1} to 3407 cm^{-1}. Interestingly, the infrared bands at 2360.17 cm^{-1}, 2853.01 cm^{-1}, and 3778.10 cm^{-1} totally vanished, and a new band appeared at 597.6 cm^{-1}, which may indicate that various functional groups were involved in the nanoparticle formation [46]. A stretching vibration of Fe-O-Fe was detected at 597.6 cm^{-1}. The Fe-O stretching band of magnetite (Fe_3O_4) is represented by the peak at 597.6 cm^{-1} [47]. This distinctive peak verified the creation of Fe_3O_4 nanoparticles, since the peaks located in the 400–600 cm^{-1} range are indicative of Fe_3O_4 [48]. Therefore, the FTIR results indicate that plant bioactive metabolites are essential to the reduction and stabilization of Fe_3O_4 nanoparticles.

3.2.2. *FTIR spectroscopy of the natural dye*

The FTIR spectra of the dye extracted from *Carica papaya* (Pawpaw) leaves are displayed in Fig. 6(b). The majority of the distinctive peaks of chlorophyll derivatives are visible in the spectra. The N—H, C—H, C=O, C=C and O=C=O groups are represented in the distinctive infrared band of chlorophylls and their derivatives [49]. Fig. 6(b) shows that the protein's N—H group is indicated by a small, intense peak at 3399 cm^{-1}, while the saturated C—H_3 vibration was seen at 2910 cm^{-1}. The O=C=O stretching of carbon dioxide is located at 2354 cm^{-1} [40] and pheophytin 'a' C=C vibrations are detected at 1629 cm^{-1}. The bending vibration of H—C-H is represented by the band at 1386.2 cm^{-1}. Additionally, stretching of C—O and C—C was also observed in the 1000 cm^{-1}–1245 cm^{-1} range [46]. The extracted dye's presence of pheophytin "a" is confirmed by the FTIR results, which are in good agreement

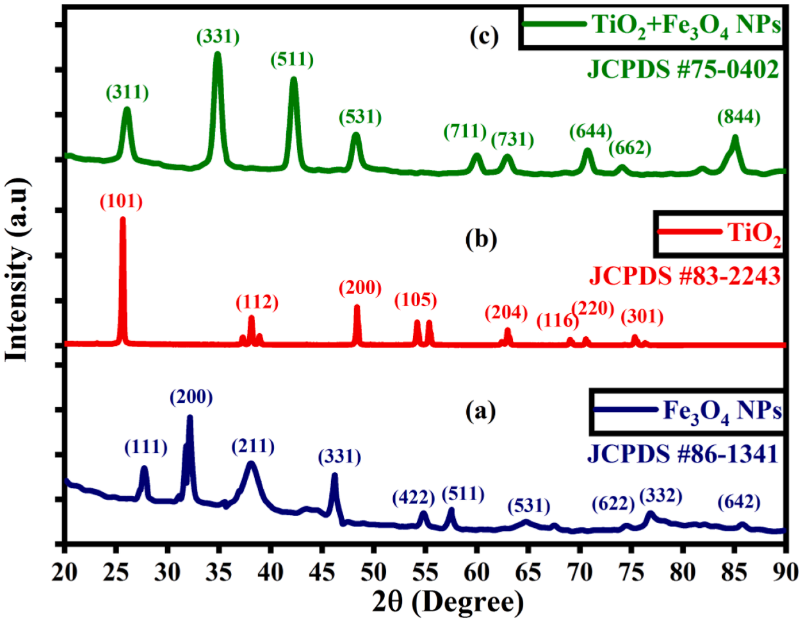

Fig. 7. XRD pattern of (a) Fe_3O_4 NPs (b) TiO_2(c) TiO_2+ Fe_3O_4 NPs.

with the UV–Vis spectral results.

3.3. Structural studies of Fe/TiO$_2$ nanoparticle

To confirm phase formation on the samples, X-ray diffraction (XRD) patterns of the green-synthesized Fe$_3$O$_4$ nanoparticle, TiO$_2$, and TiO$_2$ modified with the nanoparticle were obtained, as illustrated in Fig. 7. With the major peaks at (2θ degrees) 28.50, 32.45, 38.86, 46.94, 55.17, 57.46, 65.62, 75.15, 77.55, and 86.72, which correspond to the (111), (200), (211), (331), (422), (511), (531), (622), and (332) planes, respectively, Fig. 7(a) clearly illustrates the spinal structured magnetite. Fe$_3$O$_4$ nanoparticle index formation was determined using the JCPDS card [file no.: #86–1341], and it was found to possess a face-centered cubic (FCC) structure [50]. By using the Debye-Scherrer equation, the synthesized nanoparticle's average crystallite size —which was crystalline in nature—was calculated to be 35.13 nm [51]. The TiO$_2$ is made up of mixed anatase and rutile phases, as shown in Fig. 7(b), which correlates with the JCPDS reference pattern, card no. #83–2243. The anatase phase of TiO$_2$ is represented by the peaks observed at 2θ (degrees) values of 25.67, 38.92, 48.38, 68.72, 70.92, and 76.33, which are corresponding to the crystallographic planes (101, 112, 200, 116, 220), and (301), respectively. On the other hand, the rutile phase of TiO$_2$ is represented by the peaks at 2θ values of 54.21 and 63.00, which are ascribed to the crystallographic planes (105) and (204). It was discovered that the pattern was crystalline in nature and had a body-centered tetragonal structure. An estimate of the average crystallite size was 42.22 nm. Fig. 7(c) shows that the average crystallite size measured after the TiO$_2$ was integrated with the nanoparticle was 34.64 nm. The TiO$_2$ integrated with the nanoparticle is crystalline with a face-centered cubic structure, as shown in Fig. 7(c), and it is consistent with the JCPDS reference patterns, card number #75–0402. The rutile phase of the TiO$_2$ and the peaks attributed to the Fe$_3$O$_4$ in the nanoparticle almost exactly overlap. As a result, the peaks in the TiO$_2$ nanocomposite are identical, indicating that the Fe$_3$O$_4$ nanoparticle was successfully doped into the TiO$_2$. Fe$_3$O$_4$ nanoparticle peaks are not clearly visible, which may be related to its low concentration in TiO$_2$.

3.4. Morphological studies of Fe/TiO$_2$ nanoparticle

Fig. 8 illustrates the TiO$_2$ and Fe$_3$O$_4$ nanoparticles' surface morphologies, as well as the TiO$_2$ modified by the nanoparticles, as observed by SEM. The sample's uniformity, high stability, surface modification, and sphericality are all evident in Fig. 8(a), which may be related to the extract's stabilizing action. Iron and other component elements are confirmed to be present by the synthesized nanoparticle's Energy Dispersive Spectral analysis (EDX). Elements like Si, P, O, C, Ca, Al, Na, Mg, Fe, and K are visible in the image. The creation of Fe$_3$O$_4$ nanoparticles was confirmed by the presence of iron and oxygen. The nature of the extract used to create the nanoparticle may have contributed to the other elements' presence in the nanoparticle. Previous research has demonstrated that the use of Moringa leaf extract led to the reduction and formation of highly stable, spherical Fe$_3$O$_4$ nanoparticles with modified surfaces. Remarkably, the magnetic properties of the nanoparticle were unaffected by the plant biomolecules. Rather, they made the properties more stable against the environment and were shielded from intraparticle interactions [52]. Fig. 8(b)'s TiO$_2$ nanoparticle SEM micrograph shows the development of a porous structure. As the nanoparticle was added, the sample's surface morphology changed. As shown in Fig. 8(c), the TiO$_2$ incorporated with the extract of moringa leaves had a smoother surface morphology. There were no significant domains of aggregated particles, and the morphology became clear, homogenous, and intense. The picture demonstrated the uniform dispersion and well-formedness of the nanoparticles. Titanium and oxygen make up the TiO$_2$ nanoparticle, according to the EDX analysis of the particle. The presence of Ti, O, Al, Fe, Si, Mg, P, Ca, and C was confirmed by the EDX result for the TiO$_2$ nanocomposite. The characteristic iron (Fe) peak that was seen served as confirmation of the nanoparticle's existence. To support the structural characterizations, TEM characterizations of the nanoparticle, TiO$_2$ and TiO$_2$ nanocomposite were also performed. According to the TEM micrograph shown in Fig. 9(a), the nanoparticles are spherical in shape and have an extensive size distribution with a range of 1 to 98 nm, with the majority of them falling between 1 nm and 50 nm. This verifies that the produced nanoparticle is superparamagnetic. According to reports, Fe$_3$O$_4$ magnetic nanoparticles exhibit superparamagnetic behavior at room temperature, where they function like a permanent magnetic dipole that is easily affected by an external magnetic field when their particle size decreases significantly. Fe$_3$O$_4$ nanoparticles have a greater magnetic susceptibility and a smaller size, which makes them a viable option for integration in solar energy systems [10]. The TEM micrograph corroborates the size distribution histogram in Fig. 9(b), which displays an average particle size of 40.83 nm. Fig. 12(a)'s SAED pattern displays the nanoparticle's (111) and (200) planes. The TiO$_2$ nanoparticle's TEM image, displayed in Fig. 10(a), indicates that it has a spherical shape and a broad size distribution, ranging from 18 nm to 94 nm. The micrograph further verifies the formation of 46.6 nm-sized nanoparticles on average,

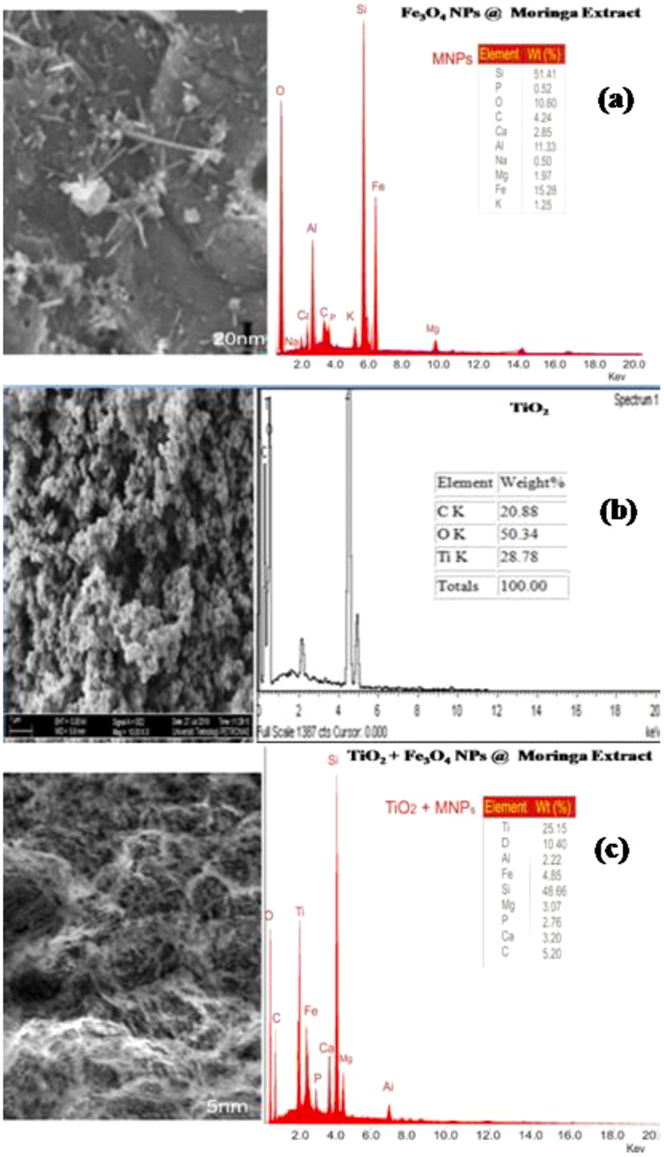

Fig. 8. SEM micrograph and EDX spectral of (a) Fe$_3$O$_4$ NPs (b) TiO$_2$ (c) TiO$_2$+ Fe$_3$O$_4$ NPs.

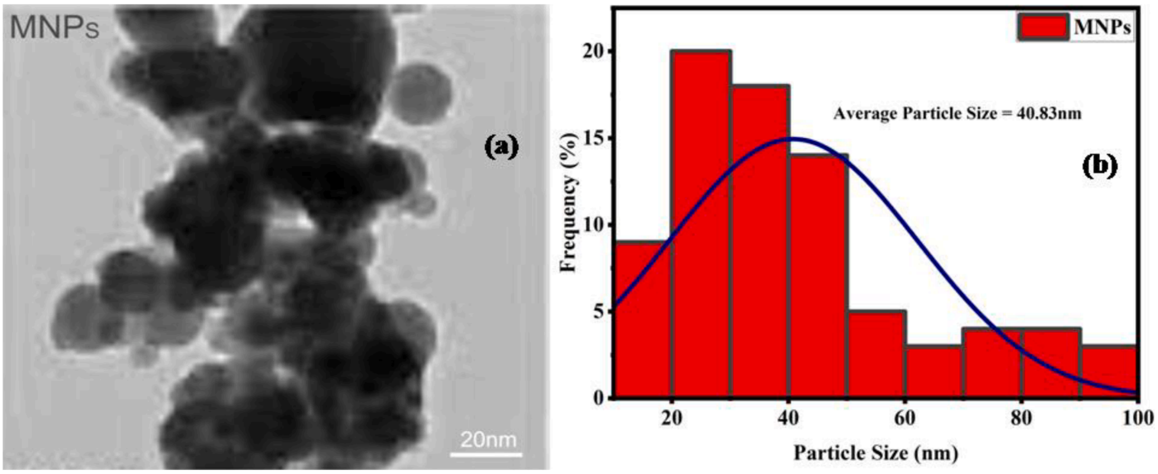

Fig. 9. (a) TEM micrograph of Fe_3O_4 nanoparticle (b) Size distribution histogram of Fe_3O_4 nanoparticle.

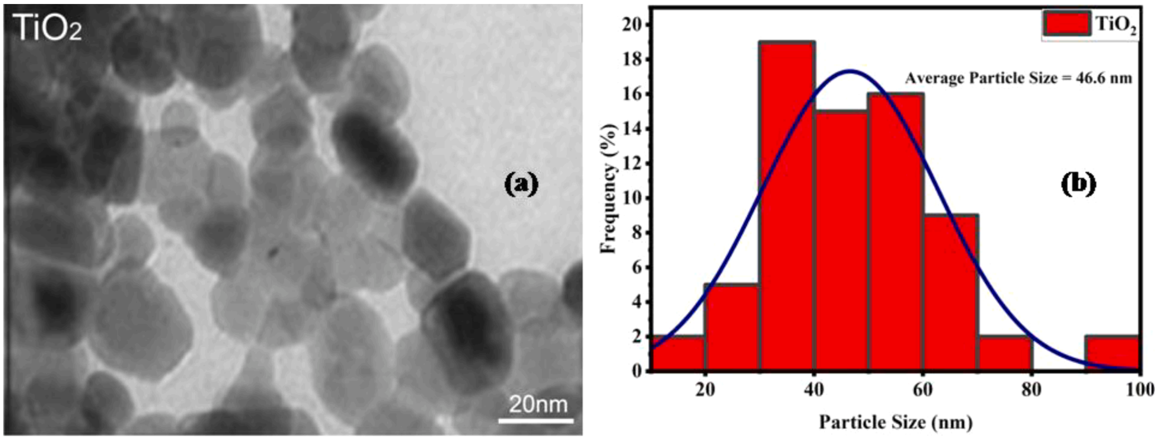

Fig. 10. (a) TEM micrograph of TiO_2 nanoparticle (b) Size distribution histogram of TiO_2 nanoparticle.

as seen by the size distribution histogram in Fig. 10(b). The TiO_2 nanoparticle's planes (101) and (112) are depicted in the SAED pattern in Fig. 12(b). The TEM image of the synthesized nanoparticle integrated with TiO_2 shown in Fig. 11(a) indicates that the nanoparticle has a spherical shape and a large number of nanoparticles within the range of 20 nm to 50 nm, along with a wide size distribution in the range of 20 nm to 80 nm. In addition, the TEM micrograph verifies the formation of 37.37 nm-sized nanoparticles, as evidenced by the size distribution histogram in Fig. 11(b). The SAED pattern in Fig. 12(c) displays the nanocomposite's (311) and (331) planes.

3.5. Photovoltaic performance of the fabricated DSSCs

The synthesized Fe_3O_4 nanoparticle was embedded in TiO_2

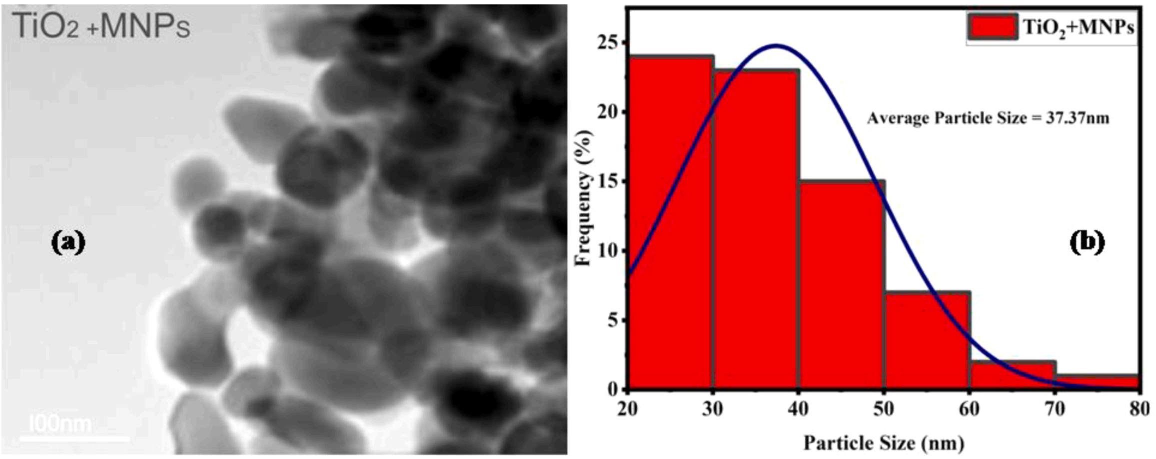

Fig. 11. (a) TEM micrograph (b) Size distribution histogram of TiO_2 incorporated with Fe_3O_4 nanoparticle.

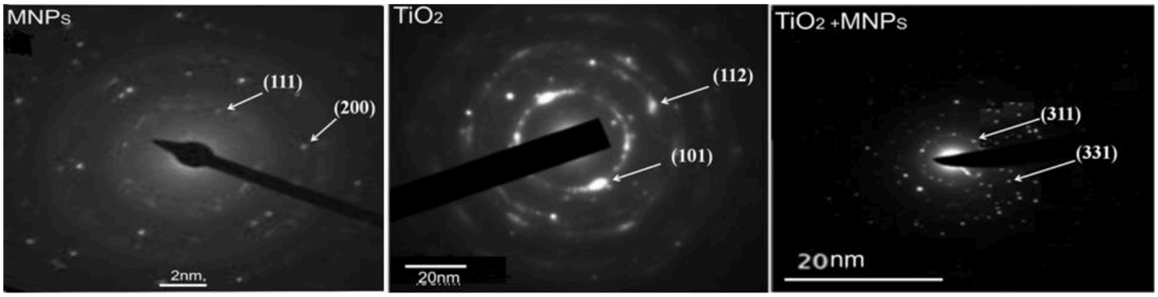

Fig. 12. SAED pattern of the (a) nanoparticle (b) TiO$_2$ (c) TiO$_2$ incorporated with Fe$_3$O$_4$ nanoparticle.

photoanode, while natural dye was used as sensitizer along with commercially available Ruthenium (N719) dye. The TiO$_2$ and modified TiO$_2$ photoanodes were used to successfully fabricate the DSSCs and their photo-electrochemical performances were examined. Fig. 13(a & b) displays current density versus voltage curves for DSSCs sensitized by natural and N719 dyes, both with and without nanoparticles. Additionally, Table 3 lists the photo-electrochemical parameters for DSSCs without nanoparticles, while Table 4 lists the parameters for DSSCs with nanoparticles. These show the energy conversion efficiency (η), fill factor (FF), open-circuit voltage (Voc), and short-circuit photocurrent density (Jsc) of the DSSCs. As can be seen in Tables 3 and 4 as well as Fig. 13(a & b), the nanoparticle increased the TiO$_2$ nanoparticle's ability to absorb the dye. With the addition of the nanoparticle, both the (Voc) and the Fill Factor improved. The short-circuit photocurrent density (Jsc) of the Ruthenium and Pawpaw dyes change from 5.1 mA to 6.1 mA and 6.6 mA to 9.5 mA, respectively, while their open-circuit voltages (Voc) change from 0.49 V to 0.72 V and 0.72 V to 0.83 V, respectively. Additionally, the efficiencies rose by a percentage of 90.1% and 89.3%, from 1.72% to 3.28% and 5.16% to 9.77%, respectively. The faster charge transfer between Fe^{2+} and Fe^{3+}, that results from Fe$_3$O$_4$ nanoparticles on the TiO$_2$ surface, which increase additional electron conduction paths and limit the condition of electron recombination, may be the cause of the improved photovoltaic performance [26]. The photo-induced charge carriers' electron sink was the nanoparticle embedded in TiO$_2$ [53]. This led to a noticeable increase in photocurrent by somewhat increasing the dye molecules' optical absorption. The incident photons were sufficiently absorbed by the TiO$_2$ to reach or surpass the band-gap energy. Fe$_3$O$_4$ nanoparticle incorporation into TiO$_2$led to increased Jsc and decreased charge transfer resistance because of improved charge transport. Higher Voc was the outcome of suppressed recombination, as evidenced by the longer charge carrier lifetime [54]. The incorporation of the Fe$_3$O$_4$ nanoparticle in the TiO$_2$ layer greatly improved the charge transfer in the devices and concurrently declined the recombination of charge carriers, which also enhanced the electronic conversion efficiency, according to a comparison of the Jsc and Voc values of the modified devices with those of the DSSCs with bare TiO$_2$ photoanode [24]. Additionally, in comparison to the research conducted by J-C Chou et al. [23], who used ruthenium-based dye to investigate the photovoltaic properties of dye-sensitized solar cells based on Fe$_3$O$_4$-TiO$_2$ composited photoanode, and who obtained the photovoltaic conversion efficiency of 3.54% based on Fe$_3$O$_4$-TiO$_2$ composited photoelectrode and 2.35% of DSSC based on TiO$_2$ pure photoelectrode, the green-synthesized Fe$_3$O$_4$ nanoparticle could be suggested as a promising and superior nanomaterial for use in DSSC.

Table 3
Photo-electrochemical characteristics of DSSCs without nanoparticles sensitized by natural and N719 dyes.

Sample	Active Area (cm^2)	V$_{OC}$ (V)	J$_{SC}$ (mA/cm^2)	FF (%)	Efficiency, η (%)
Pawpaw	0.64	0.49	5.1	30.2	1.72
Ruthenium	0.64	0.72	6.6	45.0	5.16

Table 4
Photo-electrochemical characteristics of DSSCs with nanoparticles sensitized by natural and N719 dyes.

Sample	Active Area (cm^2)	V$_{OC}$ (V)	J$_{SC}$ (mA/cm^2)	FF (%)	Efficiency, η (%)
Pawpaw	0.64	0.72	6.1	33.2	3.28
Ruthenium	0.64	0.83	9.5	52.0	9.77

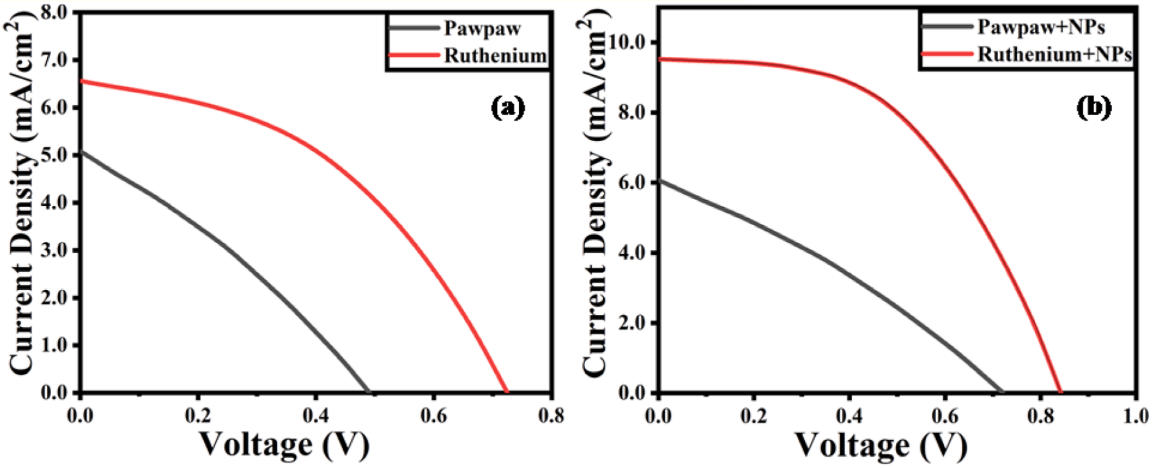

Fig. 13. Current density versus voltage curves for DSSCs sensitized by natural and N719 dyes (a) without nanoparticle (b) with nanoparticle.

4. Conclusion

It has been demonstrated that a novel green synthesis of magnetic Fe_3O_4 nanoparticles can be achieved by using extract from Moringa leaves. The absorbance in the visible range was enhanced by the nanoparticle's incorporation into TiO_2. The natural dye that was extracted showed promising qualities for use as a sensitizer in DSSC. It was found that as absorbance rose, the energy gap shrank. FTIR analyses were performed, and the findings indicated the existence of various functional groups and their potential contribution to the nanoparticle's formation. Additionally, XRD analyses were performed, and the patterns revealed that the synthesized nanoparticle had an average crystallite size of 35.13 nm, indicating that it was crystalline in nature. The well-formed and uniformly distributed nature of the nanoparticle was indicated by its morphology. We saw smoother surface morphology in the TiO_2 that was combined with the nanoparticle. The synthesized nanoparticle, TiO_2 nanoparticle, and TiO_2 nanocomposite's energy dispersive spectra (EDX) verified the presence of iron and other component elements. The formation of nanoparticles with an average size of 40.83 nm was also confirmed by the analysis of the TEM micrograph of the particle, and the SAED pattern revealed the crystallographic planes. After DSSCs were fabricated, their photo-electrochemical performances using natural and ruthenium dyes revealed that the addition of nanoparticles enhanced the efficiencies by 90.1% and 89.3%, respectively. This study demonstrated that the green-synthesized Fe_3O_4 nanoparticle integrated into the DSSC photoanode demonstrated favorable characteristics and might be suggested for use in DSSC because of its high specific surface area, biocompatibility, and good dispersion.

CRediT authorship contribution statement

Gabriel Ayinde Alamu: Writing – original draft, Visualization, Validation, Software, Methodology, Investigation, Formal analysis, Data curation, Conceptualization. **Paul Sola Ayanlola:** Writing – review & editing, Visualization, Formal analysis. **Khadijat Kuburat Babalola:** Writing – review & editing, Visualization, Formal analysis. **Oluwaseun Adedokun:** Resources, Supervision, Formal analysis, Validation, Visualization, Writing – review & editing. **Yekinni Kolawole Sanusi:** Writing – review & editing, Validation, Supervision, Resources. **Gabriel Ray Fajinmi:** Writing – review & editing, Validation, Supervision, Resources.

Declaration of competing interest

The authors declare that they have no known competing financial interests or personal relationships that could have appeared to influence the work reported in this paper.

Data availability

Data will be made available on request.

Acknowledgment

The authors acknowledge with thanks the Department of Physics and Materials Science at Kwara State University, Nigeria for the thin films deposition and IV characterizations, University Teknologi PETRONAS, Malaysia for the XRD analysis and Department of Pure and Applied Physics, LAUTECH, Nigeria for UV-vis analysis. The insightful discussions and technical assistance from members of the Nanotechnology Research Group, LAUTECH, Ogbomoso, are all gratefully acknowledged by the authors.

References

[1] J. Weiss, P. Takhistor, D.J. McClements, Functional Materials in Food Nanotechnology, J. Food Sci. 71 (9) (2006) R107–R116, https://doi.org/10.1111/j.1750-3841.2006.00195.x.

[2] V.V. Shanbhag, S.C. Prashantha, C.R. Ravi Kumar, P. Kumar, B.S. Surendra, H. Nagabhushana, D.M. Jnaneshwara, V. Revathi, Ramachandra Naik, T. S. Shashidhara, Y.G. Krupanidhi, Comparative analysis of electrochemical performance and photocatalysis of SiO_2 coated $CaTiO_3$:RE^{3+} (Dy, Sm), Li^{+} core shell nano structures, Inorg. Chem. Commun. 134 (2021) 108960, https://doi.org/10.1016/j.inoche.2021.108960.

[3] V.V. Shanbhag, S.C. Prashantha, T.R. Shashi Shekbar, H. Nagabhushana, Ramachandra Naik, K.M. Girish, S. Ashwini, D. Rangappa, D.S. Prasanna, Enhanced photoluminescence of SiO_2 coated $CaTiO_3$:Dy^{3+}, Li^{+} nanophosphors for white light emitting diodes, Ceram. Int. 47 (7) (2021) 10346–10354, https://doi.org/10.1016/j.ceramint.2020.11.077. Part B.

[4] K.M. Girish, S.C. Prashantha, R. Naik, H. Nagabhushana, H.P. Nagaswarupa, H. B. Premakumar, S.C. Sharma, K.S. Anantha Raju, Visible photon excited photoluminescence; photometric characteristics of a green light emitting Zn_2TiO_4:Tb^{3+} nanophosphor for wLEDs, Mater. Res. Express 3 3 (7) (2016) 075015, https://doi.org/10.1088/2053-1591/3/7/075015.

[5] H.S. Yogananda, R.B. Basavaraj, R. Naik, G.P. Darshan, S.C. Sharma, Daruka Prasad, H. Nagabhushana, Lysine assisted hydrothermal synthesis and formation process of MoO_3:sm^{3+} phosphors with hierarchical structures and its electron trapping luminescence properties, J. Alloys Compd. 768 (2018) 451–463, https://doi.org/10.1016/j.jallcom.2018.07.124.

[6] R. Naik, S.C. Prashantha, H. Nagabhushana, V.N. Yashwanth, K.M. Girish, H. B. Premkumar, Photoluminescent and thermoluminescent properties of low temperature synthesized Nd^{3+} doped Mg_2SiO_4 nanophosphors for display and dosimetry applications, Optik (Stuttg) 180 (2019) 8–19, https://doi.org/10.1016/j.ijleo.2018.11.069.

[7] V.V. Shanbhag, S.C. Prashantha, H. Nagabhushana, D.M. Jnaneshwara, N. Basavaraju, H.P. Nagaswarupa, K.M. Girish, Ramachandra Naik, Impacts of core shell structure on structural and photoluminescence properties of $CaTiO_3$:Sm^{3+}, Li^{+} nanoparticles for solid state display applications, Mater. Res. Express 6 (8) (2019) 085037, https://doi.org/10.1088/2053-1591/ab1d1d. Number *Mater. Res. Express* 6.

[8] L. Wang, Composite catalyst of rosin carbon/Fe_3O_4: highly efficient counter electrode for dye-sensitized solar cells, Chem. Commun. 50 (14) (2014) 1701–1703.

[9] W. Zhang, Y. Xu, H. Wang, C. Xu, S. Yang, Fe_3O_4 nanoparticles induced magnetic field effect on efficiency enhancement of P3HT: PCBM bulk heterojunction polymer solar cells, Solar Energy Mater. Solar Cells 95 (10) (2011) 2880–2885, https://doi.org/10.1016/2Fj.solmat.2011.06.005.

[10] M. Ma, Y. Zhang, Z. Guo, N. Gu, Facile synthesis of ultrathin magnetic iron oxide nanoplates by schikorr reaction, Nanoscale Res. Lett. 8 (1) (2013) 16, https://doi.org/10.1186/1556-276X-8-16.

[11] V. Madhavi, T.N.V.K.V. Prasad, A.V.B. Reddy, R.B. Ravindra, G. Madhavi, Application of phytogenic zerovalent iron nanoparticles in the adsorption of hexavalent chromium, Spectrochim. Acta A 116 (2013) 17–25, https://doi.org/10.1016/j.saa.2013.06.045.

[12] M. Herlekar, S. Barve, R. Kumar, Plant-mediated green synthesis of iron nanoparticles, J. Nanoparticles (2014) 140614, https://doi.org/10.1155/2014/140614. Article ID.

[13] J. Singh, T. Dutta, K.-H. Kim, M. Rawat, P. Samddar, P. Kumar, Green' synthesis of metals and their oxide nanoparticles: applications for environmental remediation, J. Nanobiotechnol. 16 (2018) 84, https://doi.org/10.1186/s12951-018-0408-4.

[14] E. Abbasi, S.F. Aval, A. Akbarzadeh, Dendrimer: synthesis application and properties, Nanoscale Res. Lett. 9 (2014) 247, https://doi.org/10.1186/1556-276X-9-247.

[15] Q.-U. Hassan, M.N. Chinedu, The impact of renewable energy consumption and environmental sustainability on economic growth in Africa, Energy Rep. 7 (2021) 1–9240, https://doi.org/10.1016/j.egyr.2021.05.083.

[16] K. Ibrahim, S. Khalid, K. Idrees, Nanoparticles: properties, applications and toxicities, Arabian J. Chem. 12 (7) (2019) 908–931, https://doi.org/10.1016/j.arabjc.2017.05.011.

[17] H.F. Kiwumulo, H. Muwonge, C. Ibingira, M. Lubwama, J.B. Kirabira, R. T. Ssekitoleko, Green synthesis and characterization of iron-oxide nanoparticles using *Moringa oleifera*: a potential protocol for use in low and middle income countries, BMC Res. Notes 15 (2022) 149, https://doi.org/10.1186/s13104-022-06039-7.

[18] C. Tiloke K. Anand, R.M. Gengan, A.A. Chuturgoon, *Moringa oleifera* and theirphytonanoparticles: potential anti-proliferative agents against cancer, Biomed. Pharmacother. (2018), https://doi.org/10.1016/j.biopha.2018.09.06.

[19] M. Gratzel, Solar energy conversion by dye-sensitized photovoltaic cells, Inorg. Chem. 44 (2005) 6841–6851, https://doi.org/10.1021/ic0508371.

[20] O. Adedokun, M.K. Awodele, Y.K. Sanusi, A.O. Awodugba, Natural dye extracts from fruit peels as sensitizers in ZNO-based dye-sensitized solar cells, IOP Conf. Ser. 173 (2018) 012040, https://doi.org/10.1088/1755-1315/173/1/012040.

[21] R.J. Aitken, M. Q.Chaudhry, A.B. Boxalland, M. Hull, Manufacture and use of nanomaterials: current status in the UK and global trends, Occup. Med. 56 (5) (2006) 300–306, https://doi.org/10.1093/occmed/kql051.

[22] A. Manikandan, A. Saravanan, S.A. Antony, M. Bououdina, One-pot low temperature synthesis and characterization studies of nanocrystalline A-Fe_2O_3 based dye sensitized solar cells, J. Nanosci. Nanotechnol. 15 (2015) 4358–4366, https://doi.org/10.1166/jnn.2015.9804.

[23] J. Chou, C. Chu, Y. Liao, C. Lai, Y. Lin, P. You, W. Hsu, C. Lu, Y. Nien, An investigation on the photovoltaic properties of dye-sensitized solar cells based on Fe_3O_4–TiO_2 composited photoelectrode, IEEE J. Electron Dev. Soc. (2016), https://doi.org/10.1109/JEDS.2016.2618839.

[24] A.F. Kamil, H.I. Abdullah, A. M.Rheima, S. H.Mohammed, UV-irradiation synthesized α-Fe_2O_3 nanoparticles based dye-sensitized solar cells, Mater. Today 60 (2021), https://doi.org/10.1016/j.matpr.2021.09.079. *Part 3*.

[25] U. Kannan, L. Giribabu, S. Jammalamadaka, Demagnetization field driven charge transport in aTiO_2 based dye-sensitized solar cells, Sol. Energ. 187 (2019) 281–289, https://doi.org/10.1016/j.solener.2019.05.029.

[26] L. Wang, Y. Shi, Y. Wang, H. Zhang, H. Zhou, Y. Wei, S. Tao, T. Ma, Composite catalyst of rosin carbon/Fe_3O_4: highly efficient counter electrode for dye-sensitized solar cells, Chem. Commun. 50 (14) (2014) 1701–1703, https://doi.org/10.1039/c3cc47163b.

[27] S.O. Aisida, P.A.A. K.Ugwu, A. C.Nwanya, U. Nwankwo, A.K.H. Bashir, Synthesis and characterization of iron oxide nanoparticles capped with *Moringa oleifera*: the mechanisms of formation effects on the optical, structural, magnetic and morphological properties, Mat. Today Proc. (2019), https://doi.org/10.1016/j.matpr.2020.03.167.

[28] A.H. Idris, C.A.C. Abdullah,N.A. Yusof, and M.B. Abdul-Rahman, One-pot synthesis of iron oxide nanoparticles: effect of stirring rate and reaction time on its physical characteristics. (2022). https://doi.org/10.1080/24701556.2022.2072339.

[29] I. Bibi, N. Nazar, S. Ata, M. Sultan, A. Ali, A. Abbas, K. Jilani, S. Kamal, F.M. Sarim, M.I. Khan, F. Jalal, M. Iqbal, Green synthesis of iron oxide nanoparticles using pomegranate seeds extract and photocatalytic activity evaluation for the degradation of textile dye, J. Mater. Res. Technol. 8 (2019) 6115–6124, https://doi.org/10.1016/j.jmrt.2019.10.006.

[30] S. Saravanan, R. Kato, M. Balamurugan, S. Kaushik, T. Soga, Efficiency improvement in dye-sensitized solar cells by the plasmonic effect of green synthesized silver nanoparticles, J. Sci. (2017), https://doi.org/10.1016/j.jsamd.2017.10.004.

[31] O. Adedokun, G. A.Alamu, Y. K.Sanusi, Optical studies of natural dyes and green synthesized silver nanoparticles embedded in titanium (iv) oxide for application in dye sensitized solar cells, Sci. Focus 23 (2) (2018) 22–31, https://doi.org/10.36293/sfi.2019.0004.

[32] J. Fatemeh, B. Abbas, R.K. Ali, G. Maral, A dye-sensitized solar cell based on natural photosensitizers and a PEDOT:PSS/TiO_2film as a counter electrode, Eur. Phys. J. Appl. Phys. 69 (2015) 20502, https://doi.org/10.1051/epjap/2015140370.

[33] S.S. Behera, J.K. Patra, K. Pramanik, N. Panda, H. Thatoi, Characterization and evaluation of antibacterial activities of chemically synthesized iron oxide nanoparticles, World J. Nano Sci. Eng. 2 (2012) 196, https://doi.org/10.4236/wjnse.2012.24026.

[34] M.G. Balamurughan, S. Mohanraj, S. Kodhaiyolii, V. Pugalenthi, J. Chem. Pharm. Sci. 4 (2014) 201–204, https://doi.org/10.1515/gps-2017-0145.

[35] A. Yardily, N. Sunitha, Green synthesis of iron nanoparticles using hibiscus leaf extract, characterization, antimicrobial activity, Int. J. Sci. Res. Rev. 8 (7) (2019), https://doi.org/10.1155/2022/5474645.

[36] H.S. Chen, W.C. Chang, C. Su, Carbene-based ruthenium photosensitizers, Dalton Trans. 40 (25) (2011) 6765–6770, https://doi.org/10.1039/c1dt10072f.

[37] S. Ito, T.N. Murakami, P. Comte, P. Liska, C. Grätzel, M.K. Nazeeruddin, M. Grätzel, Fabrication of thin film dye sensitized solar cells with solar to electric power conversion efficiency over 10%, Thin Solid Films 516 (14) (2008) 4613–4619, https://doi.org/10.1016/j.tsf.2007.05.090.

[38] K.M. Kumar, B.K. Mandal, M. Sinha, V. Krishnakumar, Terminalia chebula mediated green and rapid synthesis of gold nanoparticles, Spectrochim. Acta A 86 (2012) 490–494, https://doi.org/10.1016/j. saa.2011.11.001.

[39] A. Bankar, B. Joshi, A. Ravi Kumar, S. Zinjarde, Banana peel extract mediated novel route for the synthesis of silver nanoparticles, Colloids Surf. A Physicochem. Eng. Asp. 368 (2010) 58–63, https://doi.org/10.1016/j.colsurfa.2010.07.024.

[40] https://www.sigmaaldrich.com/US/en/technical-documents/technical-article/analytical-chemistry/photometry-and-reflectometry/ir-spectrum-table.

[41] Y. Cai, Y. Shen, A. Xie, Green synthesis of soya bean sprouts-mediated superparamagnetic Fe_3O_4 nanoparticles, J. Magn. Magn. Mater. 322 (2010) 2938–2943, https://doi.org/10.1016/j.jmmm.2010.05.009. https://ui.adsabs.harvard.edu/link_gateway/2010JMMM..322.2938C/.

[42] M.F. Zayed, W.H. Eisa, A.A. Shabaka, Malva parviflora extract assisted green synthesis of silver nanoparticles, Spectrochim. Acta A 98 (2012) 423–428, https://doi.org/10.1016/j.saa.2012.08.072.

[43] A. Demir, R. Topkaya, A. Baykal, Green synthesis of superparamagnetic Fe_3O_4nanoparticles with maltose: its magnetic investigation, Polyhedron 65 (2013) 282–287, https://doi.org/10.1016/j.poly.2013.08.041.

[44] Y.P. Yew, K. Shameli, M. Miyake, Green synthesis of magnetite (Fe_3O_4) nanoparticles using seaweed (*Kappaphycusalvarezii*) extract, Nanoscale Res. Lett. 11 (2016) 1–7, https://doi.org/10.1186/s11671-016-1498-2.

[45] L.P. Donald, M.L. Gary, S.K. George, and A.V. James, *Introduction to spectroscopy*, 5th ed., Cengage Learning: Boston, MA (2014). ISBN-13:978-9381466476.

[46] I.H. Kim, E.J. Park, C.H. Park, S.H. Han, H.O. Seo, Y.D. Kim, Catal. Today 295 (2017) 54–64, https://doi.org/10.1515/gps-2017-0145.

[47] M.M. Rahman, S.B. Khan, A. Jamal, M. Faisal, and A.M. Aisiri, In nanotechnology and nanomaterials, Eds., In Tech: London (2011). https://doi.org/10.1016/j.arabjc.2016.10.004.

[48] R. Yuvakkumar, S.I. Hong, Advanced Materials Research, 1051, Trans Tech Publications, Switzerland, 2014, pp. 39–42, https://doi.org/10.13005/ojc/340547.

[49] V. Shanmugan, S. Manoharan, A. Sharafali, S. Anandan, R. Murugan, Green grasses as light harvesters in dye-sensitized solar cells, Spectrochim. Acta part A 135 (2015) 947–952, https://doi.org/10.1016/j.saa.2014.07.096.

[50] S. Shukla, A. Jadaun, V. Arora, R.K. Sinha, N. Biyani, V. Jain, In vitro toxicity assessment of chitosan oligosaccharide-coated iron oxide nanoparticles, Toxicol. Rep. 2 (2015) 27–39, https://doi.org/10.1016/j.toxrep.2014.11.002.

[51] Y.C. Chang, D.H. Chen, Preparation and adsorption properties of monodispersed chitosan-bound Fe_3O_4 magnetic nanoparticles for removal of Cu(II) ions, J. Colloid Interface Sci. 283 (2005) 446–451, https://doi.org/10.1016/j.jcis.2004.09.010.

[52] M. Latorre-Sanchez, A. Primo, H. Garcia, Green synthesis of Fe_3O_4 nanoparticles embedded in a porous carbon matrix and its use as anode material in li-ion batteries, J. Mater. Chem. 22 (2012) 21373–21375, https://doi.org/10.1039/C2JM34978G.

[53] S.J. Lin, K.C. Lee, J.L. Wu, J.Y. Wu, Plasmon-enhanced photocurrent in dye-sensitized solar cells, Sol. Energy 86 (2012) 2600–2605, https://doi.org/10.1016/j.solener.2012.05.027.

[54] C. Fengshi, Z. Shixin, Y. Zhihao, Effect of magnetic gamma-iron oxide nanoparticles on the efficiency of dye-sensitized solar cells, RSC Adv. 5 (2015) 42869–42874, https://doi.org/10.1039/C5RA05936D.